Dissipativity Robustness Enhancement for LCL-Filtered Grid-Connected VSCs With Multisampled Grid-Side Current Control

He, Shan; Yang, Zhiqing; Zhou, Dao; Wang, Xiongfei; W. De Doncker, Rik; Blaabjerg, Frede

Published in:
I E E E Transactions on Power Electronics

DOI (link to publication from Publisher):
10.1109/TPEL.2022.3218378

Publication date:
2023

Document Version
Accepted author manuscript, peer reviewed version

Dissipativity Robustness Enhancement for LCL-Filtered Grid-Connected VSCs with Multi-Sampled Grid-Side Current Control

Shan He, *Student Member, IEEE*, Zhiqing Yang, *Member*, *IEEE*, Dao Zhou, *Senior Member*, *IEEE*, Xiongfei Wang, *Senior Member*, *IEEE*, Rik W. De Doncker, *Fellow*, *IEEE*, and Frede Blaabjerg, *Fellow*, *IEEE*

***Abstract*—Capacitor current active damping is a common method to achieve dissipation for LCL-filtered grid-connected converters using grid-side current control. However, the dissipative characteristic of converter output admittance near the critical frequency can easily be jeopardized by the filter parameter deviation. Besides, the grid voltage feedforward is often overlooked when designing dissipativity, which is however preferred to improve transient performance. To tackle these challenges, a multi-sampled current control scheme is proposed in this paper. By combining the capacitor current active damping and the capacitor voltage feedforward, not only the dissipation can be achieved below the Nyquist frequency, but also the dissipativity robustness against the filter parameter deviation is enhanced. Besides, the LCL-filter resonant frequency can be designed near the critical frequency, which simplifies the internal stability design. Finally, the effectiveness of the proposed method is verified through the experiments.**

***Index Terms*—Multi-sampling pulse width modulation, grid-side current control, LCL-filter parameter deviation, dissipation, grid voltage feedforward.**

I. Introduction

Increasing the integration of renewables has been regarded as a critical pathway to de-carbonize the power system [1]. As a bridge between the renewables and the power grid, LCL-filtered grid-connected voltage source converters (VSCs) are of importance to fulfill efficient and reliable power conversion [2]. A typical control structure of a grid-connected VSC requires a phase-locked loop (PLL) and an alternating current controller (ACC) to meet the grid codes. Outer loops such as the voltage and power control loops are also required in various applications [3]. In light of the controller design, a high-bandwidth ACC is required to achieve a fast current regulation [4]. In addition, the bandwidth of the PLL and outer loops should be low enough to decouple the dynamics with ACC [5]. Nevertheless, the control delay affects the bandwidth design of ACC and the VSC-grid interactive stability in the high-frequency range [6], which is the main focus of this paper.

According to the admittance-based stability criterion, the VSC control system can be represented as a current source with an output admittance in parallel. To guarantee the system stability, a stable current source is first required, which has been widely researched previously [7]. Besides, the ratio of the VSC output admittance to the grid admittance should meet the Nyquist criterion. However, the inevitable control delay often leads to a phase difference exceeding 180°, which results in an unstable system [8].

For the pulse width modulation (PWM) based digital control, single-sampling and double-sampling are the most used sampling methods whose control delay is equal to 1.5 sampling periods [9]. As an extension of the admittance shaping, the passivity-based current control is a promising solution to tackle the VSC-grid interactive instability challenge. In addition to a stable ACC, the real part of VSC output admittance should be non-negative at all frequencies [10]. However, the pure passivity is impossible to obtain, and the upper boundary of the dissipative region is set to the Nyquist frequency [11]. Consequently, the VSC-grid interactive stability can be secured regardless of the grid admittance.

In terms of the single-loop grid-side current control, a non-dissipative region occurs between the anti-resonant frequency and the critical frequency [12]. Hence, extra damping is required to enhance the dissipativity up to the Nyquist frequency. A negated Euler derivative term is inserted in parallel with the proportional resonant (PR) controller to remove the non-dissipative region [13]. The capacitor current active damping (CCAD) is another effective alternative, and the damping coefficient is derived based on the dissipative characteristic of the VSC output admittance at the critical frequency [14]. Besides, the capacitor voltage feedforward (CVF) can also be considered to achieve dissipation [15].

However, the filter parameter deviation can easily introduce a non-dissipative region near the critical frequency when using the CCAD, where the damping coefficient is replaced by a digital filter [16-17]. However, the anti-resonance frequency of the LCL filter shall be constrained to a specific range, which limits the design of the converter-side

This work was supported by the Reliable Power Electronics-Based Power System (REPEPS) project at the Department of AAU Energy, Aalborg University, as a part of the Villum Investigator Program funded by the Villum Foundation. (*Corresponding author*: *Zhiqing Yang*)

S. He, D. Zhou, X. Wang, and F. Blaabjerg are with AAU Energy, Aalborg University, Aalborg 9220, Denmark (e-mail: she@energy.aau.dk, zda@energy.aau.dk, xwa@energy.aau.dk, fbl@energy.aau.dk).

R. W. De Doncker is with the E. ON Energy Research Center, Institute for Power Generation and Storage Systems, RWTH Aachen University, Aachen 52074, Germany (e-mail: post_pgs@eonerc.rwth-aachen.de).

Z. Yang is with School of Electrical Engineering and Automation, Hefei University of Technology, Hefei 230009, China (e-mail: zhiqing.yang@hfut.edu.cn).

inductor and the filter capacitor [13, 15, 16]. In addition, the grid voltage feedforward is often ignored when designing the high-frequency dissipativity, hence the transients during the start-up or grid disturbances cannot be addressed [18-19].

To overcome the above-mentioned challenges, a multi-sampled current control scheme is proposed combining the CCAD and CVF, and its advantages are summarized as follows:

a) The dissipative range of the VSC output admittance is optimized up to the Nyquist frequency, and the transient performance is improved by adding CVF.

b) The dissipativity near the critical frequency can be secured considering the filter parameter deviation, where the LCL-filter anti-resonant frequency design is not constrained.

c) The LCL-filter resonant frequency is allowed to be near the critical frequency regardless of the filter parameter deviation, which simplifies the internal stability design.

The rest of this paper is organized as follows. In Section II, a detailed system model is derived for a grid-connected VSC with a single-loop grid-side current control. In terms of filter parameter deviations, the non-dissipative regions are investigated when using regular sampling and multi-sampling. To enhance the dissipativity robustness against filter parameter deviation, a multi-sampled damping scheme using the CCAD and CVF is proposed in Section III. The internal stability of the proposed control scheme is examined in Section IV. Experimental results are presented in Section V, and conclusions are drawn in Section VI.

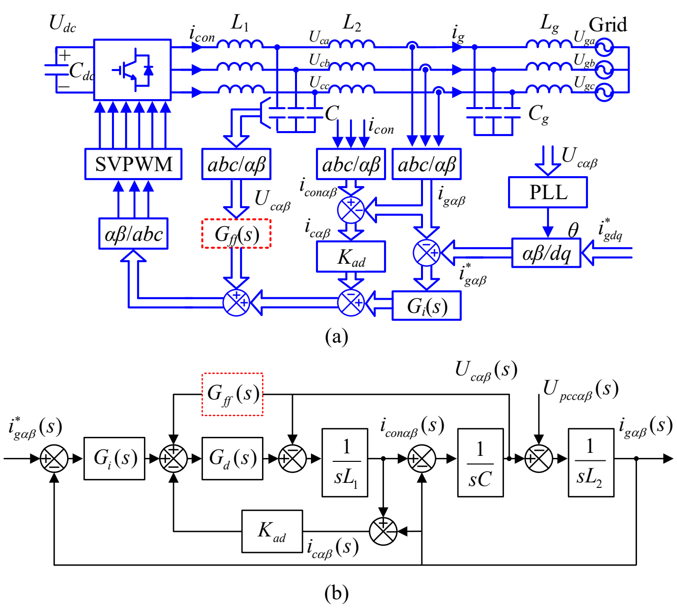

Fig. 1. Current control diagram of a three-phase grid-connected VSC. (a) Three-phase control diagram. (b) General current control model.

II. Dissipativity Analysis of Single-Loop Control

The system modeling is presented for the grid-connected VSC with the single-loop grid-side current control. Based on the system modeling, the dissipativity is analyzed considering different sampling rates and the filter parameter deviations.

A. System model

The investigated three-phase grid-connected VSC with the grid-side current control is illustrated in Fig. 1(a), where U_g is the grid voltage, U_c is the capacitor voltage, U_{dc} is the dc-link voltage, i_{con} is the converter-side current, i_g is the grid-side current, i_c is the capacitor current, and C_g and L_g are the grid impedance. An LCL filter is inserted to suppress the switching harmonics, where L_1 is the converter-side inductance, L_2 is the grid-side inductance, and C is the filter capacitance.

According to the general control diagram of the ACC depicted in Fig. 1(b), the grid-side current using the single-loop control is obtained as

$$i_g(s) = G_{cl}(s) i_g^*(s) - Y_o(s) U_{pcc} \tag{1}$$

where $G_{cl}(s)$ is the closed-loop transfer function and $Y_o(s)$ is the VSC output admittance seen from the point of common coupling (PCC). The expressions of $G_{cl}(s)$ and $Y_o(s)$ are

$$G_{cl}(s) = \frac{G_i(s)G_d(s)}{s^3 L_1 L_2 C + s(L_1 + L_2) + G_i(s)G_d(s)} \tag{2}$$

$$Y_o(s) = \frac{s^2 L_1 C + 1}{s^3 L_1 L_2 C + s(L_1 + L_2) + G_i(s)G_d(s)}. \tag{3}$$

$G_d(s)$ models the control delay T_d which is given as

$$G_d(s) = e^{-sT_d}. \tag{4}$$

$G_i(s)$ is the PR controller, which is

$$G_i(s) = K_p + K_r \omega_{rc} \frac{s\cos\varphi_g - \omega_g \sin\varphi_g}{s^2 + \omega_{rc}s + \omega_g^2} \tag{5}$$

where ω_g, ω_{rc}, φ_g, K_p, and K_r represent the grid fundamental angle frequency, the cut-off angle frequency of the resonant controller, the compensation angle of the resonant controller, the proportional and the resonant controller gain, respectively.

B. Single/double-sampling control

According to the passivity-based theory, a grid-connected VSC can be stabilized if the following two constraints are satisfied. First, the closed-loop transfer function in (2) should be stable, which will be discussed in Section IV. Second, the phase of $Y_o(s)$ should be within [−90°, 90°], i.e., the real part of $Y_o(j\omega)$ should be non-negative. Since the control delay mainly affects the dissipation in the high-frequency range, the resonant controller can be temporarily neglected. The real part of the VSC output admittance is obtained as

$$\begin{gathered}\mathrm{Re}\{Y_o(j\omega)\} \approx \frac{(1 - L_1 C\omega^2)K_p \cos(\omega T_d)}{A^2 + B^2} \\ \begin{cases} A = K_p \cos(\omega T_d) \\ B = \omega^3 L_1 L_2 C - \omega(L_1 + L_2) + K_p \sin(\omega T_d) \end{cases}\end{gathered} \tag{6}$$

Based on (6), a non-dissipative region exists between the anti-resonant frequency f_{anti} and the critical frequency f_{crit}, which are given as

$$f_{non-dissipative} = (f_{crit}, f_{anti}) \text{ or } (f_{anti}, f_{crit}) \tag{7}$$

$$f_{anti} = \frac{1}{2\pi}\sqrt{\frac{1}{L_1 C}} \tag{8}$$

This article has been accepted for publication in IEEE Transactions on Power Electronics. This is the author's version which has not been fully edited and content may change prior to final publication. Citation information: DOI 10.1109/TPEL.2022.3218378

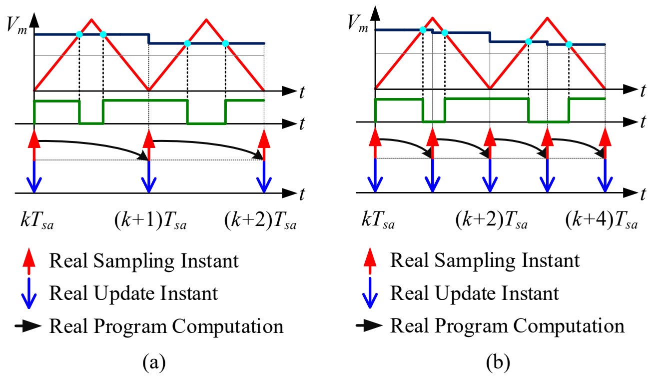

Fig. 2. Regular sampling PWM. (a) Single-sampling PWM. (b) Double-sampling PWM.

$$f_{crit} = \frac{1}{4T_d}. \tag{9}$$

For the single- and double-sampling PWM shown in Fig. 2, the control delay T_d is $1.5T_{sw}$ and $0.75T_{sw}$, where T_{sw} is the switching period. Considering a constant anti-resonant frequency, the non-dissipative boundary using single-sampling PWM is $f_{sw}/6$, while the boundary using the double-sampling PWM is $f_{sw}/3$. Hence, reducing the control delay jeopardizes the dissipation of single-loop control especially when $f_{anti}<f_{crit}$, which imposes conflicts in designing a high-bandwidth ACC.

C. Multi-sampling control

Multi-sampling PWM is a potential candidate to reduce the control delay, which has been widely used in DC-DC converters, DC-AC converters, and motor drives to improve the control bandwidth [20]. The general multi-sampling PWM is shown in Fig. 3, where the state variable is sampled and the duty cycle is updated multiple times within one switching period. Specifically, the control delay $T_{d,MS}$ is inversely proportional to the sampling rate N [21], which is given as

$$T_{d,MS} = \underbrace{\frac{1.5}{N}T_{sw}}_{\text{Computation delay + PWM delay}}. \tag{10}$$

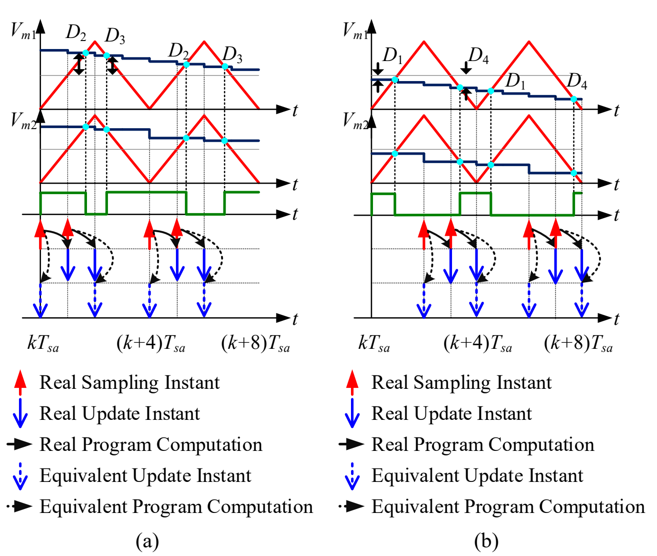

Fig. 3. General multi-sampling PWM. (a) Positive half cycle of modulation signal. (b) Negative half cycle of modulation signal.

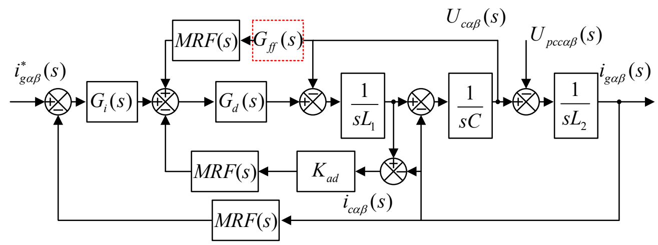

Fig. 4. General multi-sampled grid-side current control diagram (MRF: modified repetitive filter).

Since only two duty cycles are effective within one switching period, based on the voltage-second equivalence, the multi-sampling PWM is equal to a double-sampling PWM with the sampling instant shift and the update instant shift. That is to say, the Nyquist frequency for multi-sampling PWM is equal to the switching frequency [22]. However, to suppress the low-order aliasing caused by the sampled switching harmonics, a modified repetitive filter (MRF) should be inserted in the feedback path [23-24], as shown in Fig. 4. The MRF contains a compromised moving average filter (CMAF) and a delay compensator, which is given as

$$MRF(s) = \underbrace{\frac{2}{N}\frac{1-e^{-NsT_{sa}}}{1-e^{-2sT_{sa}}}}_{\text{CMAF}} \underbrace{\frac{1-r^N}{1-r^2}\frac{1-r^2e^{-2sT_{sa}}}{1-r^Ne^{-NsT_{sa}}}}_{\text{Delay Compensator}} \approx e^{-\frac{sT_{sw}}{4}} \tag{11}$$

where $r \in (0, 1)$ is the attenuation factor. There is a trade-off between the delay compensation performance and high-frequency noise suppression ability in terms of the variation in r. For the practical implementation, the MRF in (11) can be represented in z-domain, and its expression is given as

$$MRF(z) = \underbrace{\frac{2}{N}\frac{1-z^{-N}}{1-z^{-2}}}_{\text{CMAF}} \underbrace{\frac{1-r^N}{1-r^2}\frac{1-r^2z^{-2}}{1-r^Nz^{-N}}}_{\text{Delay Compensator}} \approx z^{-\frac{N}{4}} \tag{12}$$

The detailed implementation diagram of MRF in microprocessor is presented in Fig. 5. Consequently, the total loop delay including the control delay and the MRF delay is

$$T_{d,MS-MRF} = \underbrace{\frac{1.5}{N}T_{sw}}_{\text{Computation delay + PWM delay}} + \underbrace{\frac{T_{sw}}{4}}_{\text{MRF delay}} = \frac{6+N}{4N}T_{sw}. \tag{13}$$

Substituting (13) into (9), the non-dissipative boundary ($\frac{N}{6+N}f_{sw}$) will be further extended when increasing the sampling rate. Similar to the analysis in single/double-sampling, extra damping is required to achieve dissipation.

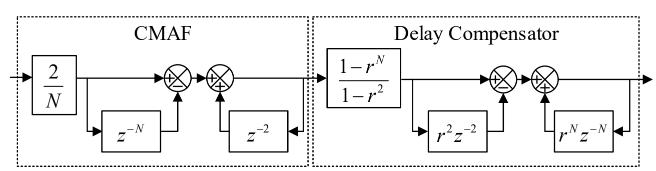

Fig. 5. Detailed implementation of modified repetitive filter (CMAF: compromised moving average filter).

D. Comparison

System specifications of the investigated grid-connected VSC are shown in Table I. The real part of the VSC output admittance is presented in Fig. 6, where different sampling rates and ±20% filter parameter deviation are considered. The

This article has been accepted for publication in IEEE Transactions on Power Electronics. This is the author's version which has not been fully edited and content may change prior to final publication. Citation information: DOI 10.1109/TPEL.2022.3218378

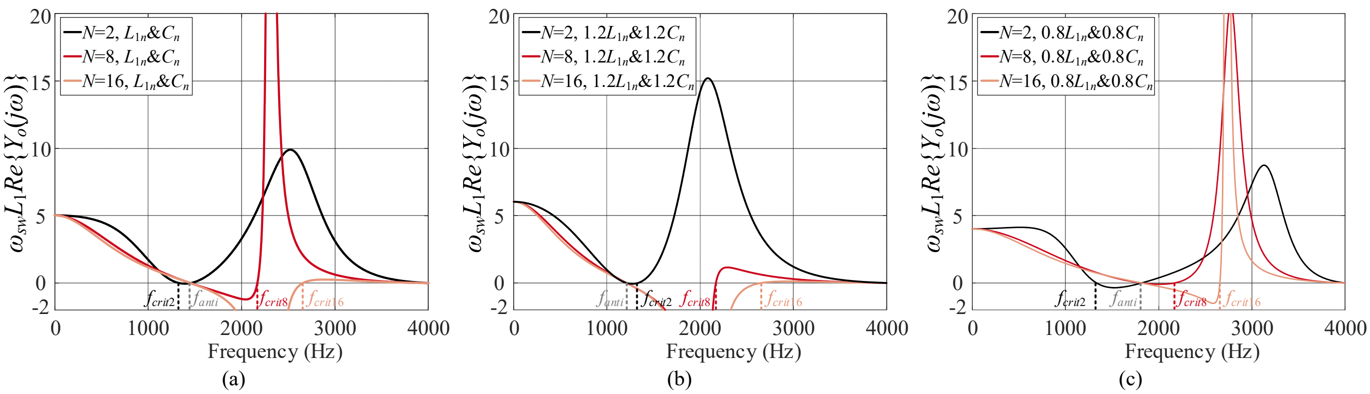

Fig. 6. Re$\{Y_o(j\omega)\}$ of single-loop control using double-sampling (N=2), eight-sampling (N=8), and sixteen-sampling (N=16). (a) With nominal values of L_1 and C. (b) With a +20% deviation of L_1 and C. (c) With a −20% deviation of L_1 and C.

TABLE I
MAIN PARAMETERS OF A THREE-PHASE GRID-CONNECTED VSC

Symbol	Description	Value	Symbol	Description	Value
System Parameters					
P_o	Output power	7 kW	U_g	Grid phase voltage (RMS)	220 V
U_{dc}	DC-link voltage	700 V	f_{sw}	Switching frequency	4 kHz
N	Sampling rate	2/8/16	K_p	Proportional controller gain	20 Ω
K_r	Resonant controller gain	1000 Ω/s	K_{ff}	Proportional feedforward coefficient	0.9
r_8	Attenuation factor	0.6	r_{16}	Attenuation factor	0.8
LCL Filter-I					
L_1	Converter-side inductance	4 mH	L_2	Grid-side inductance	2 mH
C	Filter capacitance	3 μF	f_r	Resonant frequency	2517 Hz
f_{anti}	Anti-resonant frequency	1453 Hz	K_{ad2}	Damping coefficient	-3.7 Ω
K_{ad8}	Damping coefficient	11.9 Ω	K_{ad16}	Damping coefficient	15.0 Ω

resonant controller is ignored for the analysis in the high-frequency range. According to (7), setting the anti-resonant frequency close to the critical frequency can help to enhance the dissipativity. As depicted in Fig. 6(a), the anti-resonant frequency f_{anti} is 1453 Hz for LCL Filter-I and the critical frequency f_{crit2} for double-sampling is 1333 Hz. However, the dissipativity near the critical frequency can easily be affected by the filter parameter deviation, as illustrated in Fig. 6(b)-(c). If the anti-resonant frequency is higher than the critical frequency, a positive parameter deviation reduces the non-dissipative region, and vice versa. A similar conclusion can be obtained when the anti-resonant frequency is smaller than the critical frequency.

Moreover, the critical frequency of the multi-sampling PWM is higher than half of the switching frequency, and it is difficult to set the anti-resonant frequency close to the critical frequency for the multi-sampling PWM. Otherwise, the LCL-filter resonant frequency may be close to or even above the switching frequency. This is because the LCL-filter resonant frequency is larger than the anti-resonant frequency, which is

$$f_r = \sqrt{\frac{L_1+L_2}{L_2}}f_{anti}. \tag{14}$$

III. DISSIPATIVITY ENHANCEMENT

Resonances can occur in VSC-grid systems if excitations fall in the non-dissipative frequency ranges. To enhance the system dissipativity, a multi-sampling control scheme is proposed using CCAD and CVF.

A. Capacitor current active damping

CCAD is a common method to achieve dissipation below the Nyquist frequency. Herein, the capacitor current is calculated through the bias between the converter-side current and the grid-side current (see Fig. 1). Then, the VSC output admittance with the CCAD is given as

$$Y_o(s) = \frac{\overbrace{s^2L_1C+1}^{\text{Single-Loop Control}}\ \overbrace{+sG_d(s)K_{ad}C}^{\text{CCAD}}}{s^3L_1L_2C\underbrace{+s^2L_2CK_{ad}G_d(s)}_{\text{CCAD}}+s(L_1+L_2)+G_i(s)G_d(s)}. \tag{15}$$

By substituting 's=$j\omega$' into (15), the real part of the VSC output admittance is

$$\begin{gathered}\mathrm{Re}\{Y_o(j\omega)\} \approx \frac{\overbrace{(1-L_1C\omega^2)K_p\cos(\omega T_d)}^{\text{Single-loop control}}\overbrace{+K_{ad}\omega^2L_1C\cos(\omega T_d)}^{\text{CCAD}}}{A^2+B^2}\\ \begin{cases}A=-\omega^2K_{ad}L_2C\cos(\omega T_d)+K_p\cos(\omega T_d)\\ B=\omega^3L_1L_2C-\omega^2K_{ad}L_2C\sin(\omega T_d)-\omega(L_1+L_2)+K_p\sin(\omega T_d)\end{cases}.\end{gathered} \tag{16}$$

By changing the sign of Re$\{Y_o(j\omega)\}$ at the critical frequency, the damping coefficient is designed as

$$K_{ad} = K_p(1-\frac{\omega_{antinorm}^2}{\omega_{crit}^2}) \tag{17}$$

where $\omega_{antinorm}$ denotes the nominal anti-resonant angle frequency. Considering a general case of parameter deviations, i.e., L_1=kL_{1norm}, C=kC_{norm} where L_{1norm} and C_{norm} are the nominal values of converter-side inductance and filter capacitance, Re$\{Y_o(j\omega)\}$ can be simplified as

$$\mathrm{Re}\{Y_o(j\omega)\} \approx \frac{K_p\cos(\omega T_d)(1-\dfrac{k^2\omega^2}{\omega_{cri}^2})}{A^2+B^2}. \tag{18}$$

This article has been accepted for publication in IEEE Transactions on Power Electronics. This is the author's version which has not been fully edited and content may change prior to final publication. Citation information: DOI 10.1109/TPEL.2022.3218378

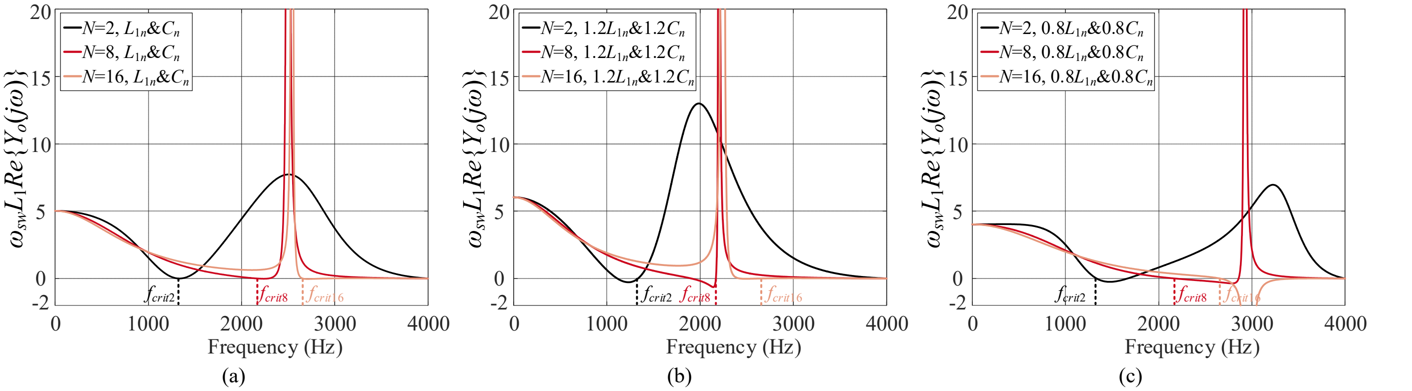

Fig. 7. Re$\{Y_o(j\omega)\}$ with capacitor current active damping using double-sampling (N=2), eight-sampling (N=8), and sixteen-sampling (N=16). (a) With nominal values of L_1 and C. (b) With a +20% deviation of L_1 and C. (c) With a −20% deviation of L_1 and C.

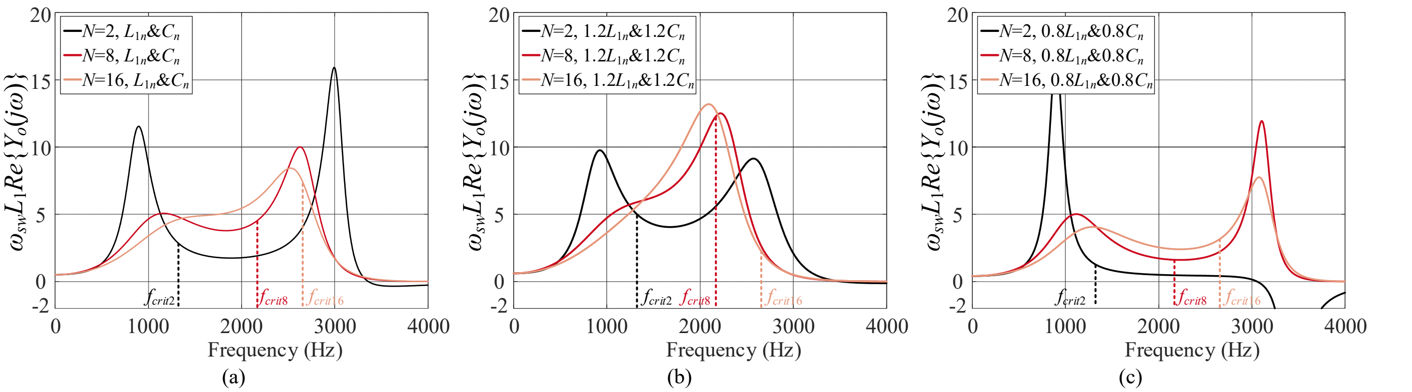

Fig. 8. Re$\{Y_o(j\omega)\}$ with capacitor current active damping and capacitor voltage feedforward using double-sampling (N=2), eight-sampling (N=8), and sixteen-sampling (N=16). (a) With nominal values of L_1 and C. (b) With a +20% deviation of L_1 and C. (c) With a −20% deviation of L_1 and C.

$$Y_o(s)=\frac{\overbrace{s^2L_1C+1}^{\text{Single-Loop Control}}\overbrace{+sG_d(s)K_{ad}C}^{\text{CCAD}}\overbrace{-K_{ff}G_d(s)}^{\text{CVF}}}{s^3L_1L_2C\underbrace{+s^2L_2CK_{ad}G_d(s)}_{\text{CCAD}}+s(L_1+L_2)\underbrace{-sL_2K_{ff}G_d(s)}_{\text{CVF}}+G_i(s)G_d(s)}. \tag{21}$$

$$\begin{gathered}\mathrm{Re}\{Y_o(j\omega)\}\approx\frac{\overbrace{(1-L_1C\omega^2)K_p\cos(\omega T_d)}^{\text{Single-loop control}}\overbrace{+K_{ad}\omega^2L_1C\cos(\omega T_d)}^{\text{CCAD}}\overbrace{-K_{ff}K_p+K_{ff}\omega L_1\sin(\omega T_d)}^{\text{CVF}}}{A^2+B^2}\\ \begin{cases}A=-\omega^2K_{ad}L_2C\cos(\omega T_d)+K_p\cos(\omega T_d)-\omega K_{ff}L_2\sin(\omega T_d)\\ B=\omega^3L_1L_2C-\omega^2K_{ad}L_2C\sin(\omega T_d)-\omega(L_1+L_2)+K_p\sin(\omega T_d)+\omega K_{ff}L_2\cos(\omega T_d)\end{cases}.\end{gathered} \tag{22}$$

According to (18), the non-dissipative region considering filter parameter variation is obtained as

$$f_{non-dissipative}=(f_{crit},\frac{f_{crit}}{k})\text{ or }(\frac{f_{crit}}{k},f_{crit}). \tag{19}$$

Ideally, there are no non-dissipative regions with the nominal filter parameters (k=1), as shown in Fig. 7(a). However, non-dissipative regions are inevitable when the parameter deviation is considered. As presented in Fig. 7(b)-(c), −20% parameter deviation can introduce a larger non-dissipative region than +20% deviation, which can also be explained using (19).

A. Capacitor current active damping and capacitor voltage feedforward

To enhance the dissipativity robustness against the filter parameter deviation and improve the transient performance simultaneously, a proportional CVF term is further introduced in addition to the CCAD. Herein, only a simple proportional feedforward function is used, which is given as

$$G_{ff}(s)=K_{ff} \tag{20}$$

where K_{ff} is the CVF coefficient. After adding the CVF, the VSC output admittance and its real part are given in (21) and (22), respectively. The dissipative characteristic at the critical frequency can be obtained by substituting 'ω=ω_{crit}' into (21), which is given as

$$\mathrm{Re}\{Y_o(j\omega_{crit})\}\approx\frac{K_{ff}L_1(\omega_{crit}-\omega_c)}{A^2+B^2}>0 \tag{23}$$

where ω_c=K_p/L_1 is the current control bandwidth. Based on (9) and (13), the critical angle frequency ω_{crit} is $0.33\omega_{sw}$ and $\frac{N}{6+N}\omega_{sw}$ for the double-sampling control and multi-sampling control, respectively. Since ω_c is usually set between $0.1\omega_{sw}$ to $0.2\omega_{sw}$, Re$\{Y_o(j\omega_{crit})\}$ can always remain positive.

The real parts of the VSC output admittance with both the

This article has been accepted for publication in IEEE Transactions on Power Electronics. This is the author's version which has not been fully edited and content may change prior to final publication. Citation information: DOI 10.1109/TPEL.2022.3218378

CCAD and CVF are presented in Fig. 8. As illustrated in Fig. 8(a), the dissipativity near the critical frequency can be enhanced with the CVF. Moreover, as shown in Fig. 8(b)-(c), the VSC output admittance can still behave dissipative around the critical frequency, even with ±20% deviation of L_1 and C. Note that the CVF coefficient should be lower than one to ensure the low-frequency dissipation [25-26].

However, a non-dissipative region still exists in the higher frequency range for the double-sampling CCAD and CVF. Taking the dissipative characteristic at the switching frequency as an example, $\mathrm{Re}\{Y_o(j\omega_{sw})\}$ is given as

$$\mathrm{Re}\left\{Y_o(j\omega_{sw})\right\}_{T_d=0.75T_{sw}} \approx \frac{-K_{ff}L_1(\omega_c+\omega_{sw})}{A^2+B^2}<0. \tag{24}$$

Due to the reduced time delay, the dissipative range can be extended up to the switching frequency using multi-sampling. When T_d is $0.5T_{sw}$, $\mathrm{Re}\{Y_o(j\omega_{sw})\}$ always remains positive because the CVF coefficient is smaller than one, which is

$$\mathrm{Re}\left\{Y_o(j\omega_{sw})\right\}_{T_d=0.5T_{sw}} \approx \frac{K_p(3-K_{ff})}{A^2+B^2}>0. \tag{25}$$

Recalling (13), the multi-sampling control delay is lower than $0.5T_{sw}$ when the sampling rate N is larger than six, and the dissipativity around the switching frequency can be further enhanced.

To summarize, the proposed multi-sampling control scheme with the CCAD and CVF can not only enhance the dissipativity robustness near the critical frequency, but also extend the dissipative range up to the switching frequency. Compared to the methods in [13, 15, 16], there are no constraints to designing the anti-resonant frequency. The dissipation near the critical frequency can still be secured even though the anti-resonant frequency is close to or equal to the critical frequency.

IV. Internal Stability of ACC

The system stability depends not only on the dissipative characteristic of the VSC output admittance, but also on the internal stability of the ACC. Conventionally, the internal stability can be designed by shaping the virtual resistance in parallel with the filter capacitor, where stringent gain margin requirements should be met at both the critical frequency and the LCL-filter resonant frequency [27]. Especially, it is difficult to secure the internal stability if the LCL-filter resonant frequency is designed close to the critical frequency. To achieve a minimum phase behavior, it is preferred to shape the virtual resistance as positive below the Nyquist frequency [28].

For the grid-side current control with the CCAD and CVF, the closed-loop transfer function between the reference current and the grid-side current is

$$G_{cl}(s)=\frac{G_i(s)G_d(s)}{s^2L_1L_2(sC+\dfrac{1}{Z_{eq}(s)})+s(L_1+L_2)+G_i(s)G_d(s)}. \tag{26}$$

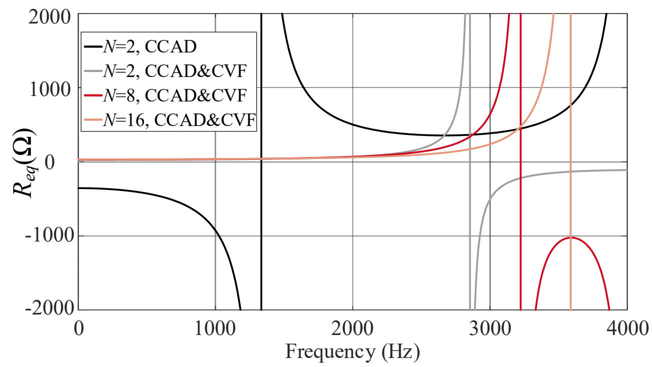

Fig. 9. Virtual resistance for different control methods. (CCAD: capacitor current active damping, CVF: capacitor voltage feedforward, N=2: double-sampling, N=8: eight-sampling, N=16: sixteen-sampling).

where $Z_{eq}(s)$ is the virtual impedance in parallel with the filter capacitor, and its expression is given as

$$Z_{eq}(s)=\frac{L_1}{(K_{ad}-\dfrac{K_{ff}}{sC})C}e^{sT_d}. \tag{27}$$

Taking the real part of (27), the virtual resistance $R_{eq}(\omega)$ is

$$R_{eq}(\omega)=\frac{L_1}{\underbrace{(1-\dfrac{\omega_{antinorm}^2}{\omega_{crit}^2})K_pC\cos(\omega T_d)}_{\text{CCAD}}+\underbrace{K_{ff}\dfrac{\sin(\omega T_d)}{\omega}}_{\text{CVF}}}. \tag{28}$$

The virtual resistances with different control schemes are presented in Fig. 9. If only the CCAD is implemented, $R_{eq}(\omega)$ remains positive in the frequency range $(0, f_{crit})$ or (f_{crit}, f_{sw}), depending on the ratio between the nominal anti-resonant angle frequency and the critical angle frequency. The positive-resistance region can be extended by adding the CVF and increasing the sampling rate. However, there is always a negative-resistance region even though the VSC output admittance is dissipative such as double-sampling CCAD, eight-sampling CCAD and CVF, and sixteen-sampling CCAD and CVF.

On the contrary, if the virtual resistance is positive below the Nyquist frequency, only the gain margin at the critical frequency should be positive, while the VSC output admittance may not be dissipative. It seems that there is no connection between the dissipativity and the sign of the virtual resistance. Specifically, depending on the anti-resonant frequency and the critical frequency, the internal stability design using the passivity-based CCAD parameters becomes a case-by-case issue [16].

To simplify the internal stability analysis, the closed-loop function with grid-side current control can be represented by the converter-side current and the capacitor voltage, which is

$$i_{con}(s)=G_{cl,con}(s)i_g^*(s)-Y_{o,con}(s)U_c(s) \tag{29}$$

where $Y_{o,con}(s)$ denotes the VSC output admittance seen from the filter capacitor. $G_{cl,con}(s)$ is the closed-loop transfer function between the reference current and the converter-side current, which is given as

$$G_{cl,con}(s)=\frac{G_i(s)G_d(s)}{sL_1+G_i(s)G_d(s)}\approx\frac{K_pG_d(s)}{sL_1+K_pG_d(s)}. \tag{30}$$

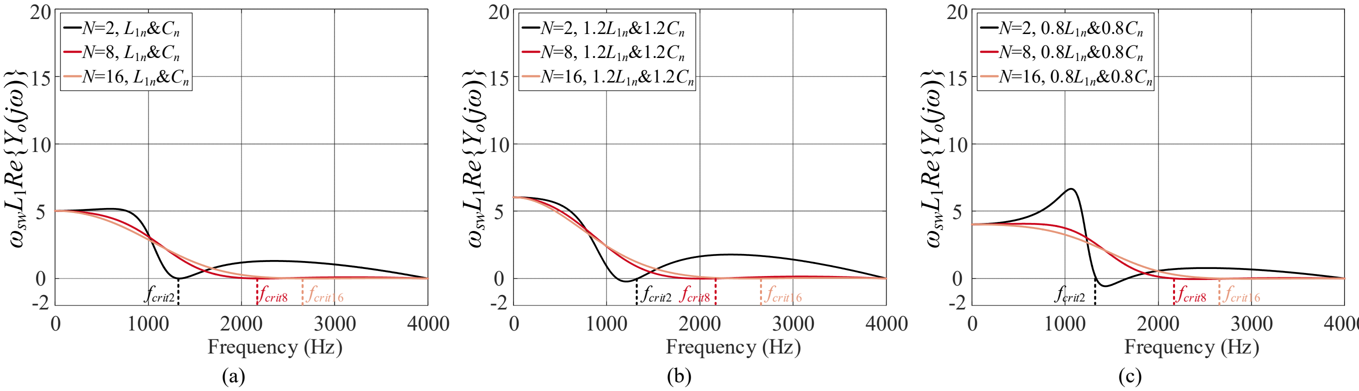

Fig. 10. Re$\{Y_{o,con}(j\omega)\}$ with capacitor current active damping using double-sampling (N=2), eight-sampling (N=8), and sixteen-sampling (N=16). (a) With nominal values of L_1 and C. (b) With a +20% deviation of L_1 and C. (c) With a −20% deviation of L_1 and C.

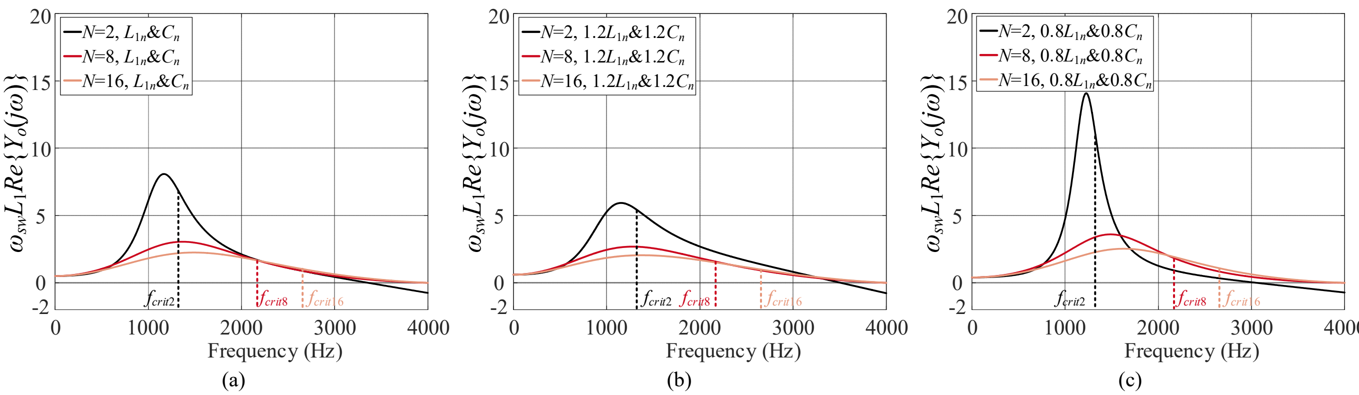

Fig. 11. Re$\{Y_{o,con}(j\omega)\}$ with capacitor current active damping and capacitor voltage feedforward using double-sampling (N=2), eight-sampling (N=8), and sixteen-sampling (N=16). (a) With nominal values of L_1 and C. (b) With a +20% deviation of L_1 and C. (c) With a −20% deviation of L_1 and C.

$$Y_{o,con}(s)=\frac{\underbrace{1-CsG_i(s)G_d(s)}_{\text{Single-loop control}}+\underbrace{(1-\frac{\omega^2_{antinorm}}{\omega^2_{cri}})K_pCsG_d(s)}_{\text{CCAD}}\underbrace{-K_{ff}(s)G_d(s)}_{\text{CVF}}}{sL_1+G_i(s)G_d(s)}\approx\frac{1-\frac{\omega^2_{antinorm}}{\omega^2_{cri}}K_pCsG_d(s)-K_{ff}(s)G_d(s)}{sL_1+K_pG_d(s)}. \tag{31}$$

$$\mathrm{Re}\{Y_{o,con}(j\omega)\}\approx\frac{K_p\cos(\omega T_d)\overbrace{-\frac{\omega^2_{antinorm}}{\omega^2_{anti}}\frac{\omega^2}{\omega^2_{cri}}K_p\cos(\omega T_d)}^{\text{CCAD}}\overbrace{-K_{ff}K_p+K_{ff}\omega L_1\sin(\omega T_d)}^{\text{CVF}}}{(K_p\cos(\omega T_d))^2+(\omega L_1-K_p\sin(\omega T_d))^2}. \tag{32}$$

In this case, L_2 and C are regarded as an equivalent grid admittance $Y_{g,eq}(s)=(1/sL_2+sC)$. By means of that, the internal stability can be analyzed through the admittance-based stability criterion using $Y_{o,con}(s)$ and $Y_{g,eq}(s)$. Compared to the closed-loop transfer function $G_{cl}(s)$ given in (26), the stability of $G_{cl,con}(s)$ can easily be secured by setting a proper bandwidth of the ACC [4], which is set to 1/5 of the switching frequency. Consequently, the internal stability of the grid-side current-controlled VSC is determined by the dissipative characteristic of $Y_{o,con}(s)$.

The expression of $Y_{o,con}(s)$ and its real part are given in (31) and (32). Considering $L_1=kL_{1norm}$ and $C=kC_{norm}$, the non-dissipative region with the CCAD is the same as (18). As depicted in Fig. 10(a), Re$\{Y_{o,con}(j\omega_{crit})\}$ with the CCAD is zero, and the dissipativity can be jeopardized by the filter parameter deviation. Consequently, it is difficult to design the internal stability when the LCL-filter resonant frequency is close to the critical frequency. After adding CVF, Re$\{Y_{o,con}(j\omega_{crit})\}$ can remain positive, which is

$$\mathrm{Re}\{Y_{o,con}(j\omega_{crit})\}\approx\frac{K_{ff}L_1(\omega_{crit}-\omega_c)}{(\omega L_1-K_p)^2}>0. \tag{33}$$

As shown in Fig. 11, the dissipativity near the critical frequency can be enhanced under a filter parameter deviation. However, a non-dissipative region occurs near the switching frequency using double-sampling, and Re$\{Y_{o,con}(j\omega_{sw})\}$ is

$$\mathrm{Re}\{Y_{o,con}(j\omega_{sw})\}_{T_d=0.75T_{sw}}\approx\frac{-K_{ff}L_1(\omega_c+\omega_{sw})}{(\omega L_1+K_p)^2}<0. \tag{34}$$

For VSCs with high pulse ratios, the LCL-filter resonant frequency is usually much lower than the switching frequency. However, the pulse ratio of high-power VSCs is typically low to save switching losses, and the LCL-filter resonant frequency can be close to the switching frequency. Hence, double-sampling control cannot ensure the internal stability for LCL-filtered VSCs with low pulse ratios, even with the CCAD and CVF. With the proposed multi-sampling CCAD and CVF, the dissipativity can be achieved below the switching frequency, which is given as

$$\mathrm{Re}\left\{Y_{o,con}(j\omega_{sw})\right\}_{T_d=0.5T_{sw}} \approx \frac{K_p(3-K_{ff})}{K_p^2+(\omega L_1)^2} > 0. \tag{35}$$

To summarize, the internal stability can easily be secured using the proposed multi-sampling control with the CCAD and CVF, which allows designing the LCL-filer resonant frequency equal or close to the critical frequency.

V. Experimental Validation

To further verify the theoretical analysis, experiments are carried out on a three-phase grid-connected VSC with an LCL filter, as shown in Fig. 12. The grid is emulated with a high-fidelity linear amplifier APS 15000. The applied half-bridge module and the control platform are a PEB-SiC-8024 module and a B-BOX RCP control platform from Imperix, respectively. The used current sensor is LEM CKSR 50-P with a bandwidth of 300 kHz. The parameters of the three-phase grid-connected VSC with LCL-Filter I and LCL-Filter II are presented in Table I and Table II.

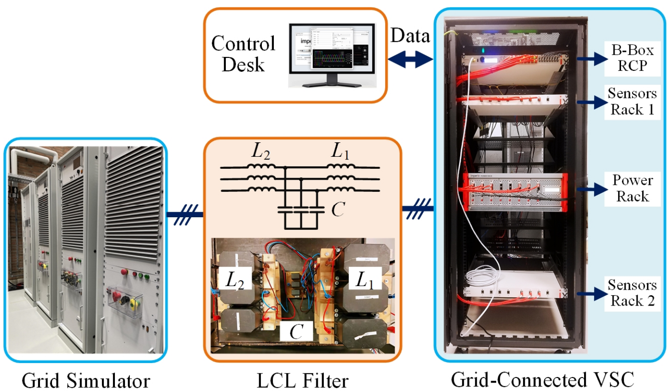

Fig. 12. A down-scaled three-phase grid-connected VSC with an LCL filter.

TABLE II
CONTROL PARAMETERS USING LCL FILTER-II

L_1	Converter-side inductance	4 mH	L_2	Grid-side inductance	2 mH
C	Filter capacitance	10 μF	f_r	Resonant frequency	1378 Hz
f_{anti}	Anti-resonant frequency	796 Hz	K_{ad2}	Damping coefficient	12.9 Ω
K_{ad8}	Damping coefficient	17.6 Ω	K_{ad16}	Damping coefficient	18.5 Ω

A. Internal stability validation

As explained previously, it is difficult to guarantee the internal stability using double-sampling grid-side current control, if the LCL-filter resonant frequency is designed close to the critical frequency. To validate the proposed multi-sampling control scheme on the internal stability design, LCL Filter-II is used whose resonant frequency (1378 Hz) is close to the double-sampling critical frequency (1333 Hz), as shown in Table II. The internal stability can be analyzed according to the VSC output admittance seen from the filter capacitor $Y_{o,con}(s)$ and the equivalent grid admittance $Y_{g,eq}(s)$.

Four cases are considered including the double-sampling CCAD with nominal values of L_1 and C, the double-sampling

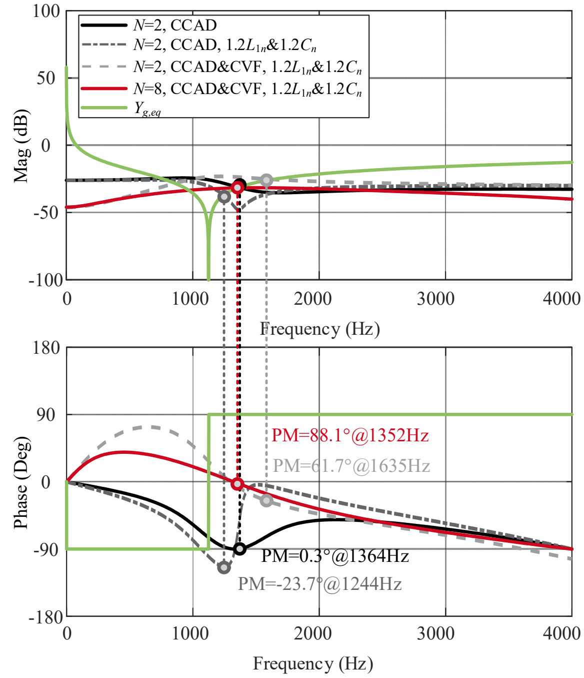

Fig. 13. VSC output admittance seen from the filter capacitor $Y_{o,con}(s)$. (CCAD: capacitor current active damping, CVF: capacitor voltage feedforward, N=2: double-sampling, N=8: eight-sampling).

CCAD, the double-sampling CCAD and CVF, and the eight-sampling CCAD and CVF with a +20% deviation of L_1 and C. Note that +20% deviation of L_1 and C in the real circuits is emulated by decreasing 20% of the nominal filter values in the CCAD coefficient (K_{ad}) calculation. Bode plots of $Y_{o,con}(s)$ and $Y_{g,eq}(s)$ are depicted in Fig. 13 for various cases. The system can be stabilized using the double-sampling CCAD with the nominal value of L_1 and C. but the phase margin (PM) is only 0.3°. Moreover, considering a +20% deviation of L_1 and C, $Y_{o\_con}(s)$ intersects with $Y_{g,eq}(s)$ in its negative-real-part region, which leads to a −23.7° PM and destabilizes the system. If the CVF is further implemented, the system becomes stabilized for both double- and eight-sampling controls, since the dissipativity near the critical frequency is enhanced. In addition, the eight-sampling CCAD and CVF can achieve a larger PM than the double-sampling control.

The experimental results of the double-sampling CCAD with nominal values of L_1 and C are shown in Fig. 14(a). The VSC starts at 40 ms, and the dc-link capacitor is charged to 700 V in the next 40 ms. The reference current steps from 0 A to 15 A (rated current) at 80 ms. It can be seen that a high transient start-up current occurs without the CVF, which may trigger the over-current protection. As depicted in Fig. 14(b), the system becomes destabilized with a +20% deviation of L_1 and C, which is consistent with the theoretical analysis in Fig. 12. By further implementing the CVF, not only the transient current during the start-up is suppressed, but also the internal system stability can be secured, as illustrated in Fig. 14(c)-(d) for both the double- and eight-sampling control.

B. VSC-grid interactive stability validation

To ensure the internal stability for double-sampling CCAD, LCL Filter-I is used where the resonant frequency (2517 Hz)

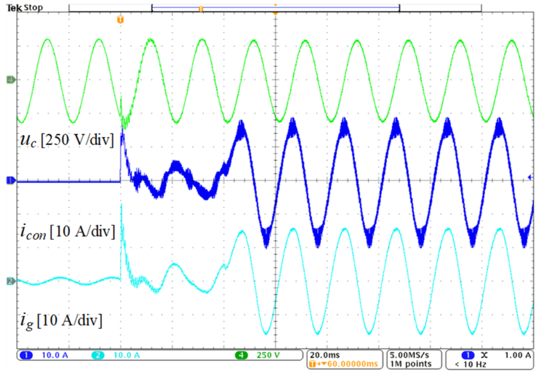

(a)

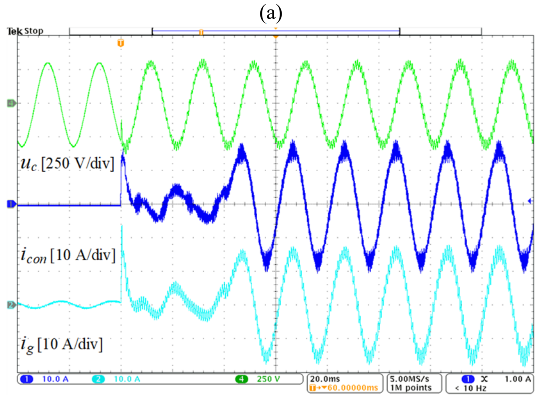

(b)

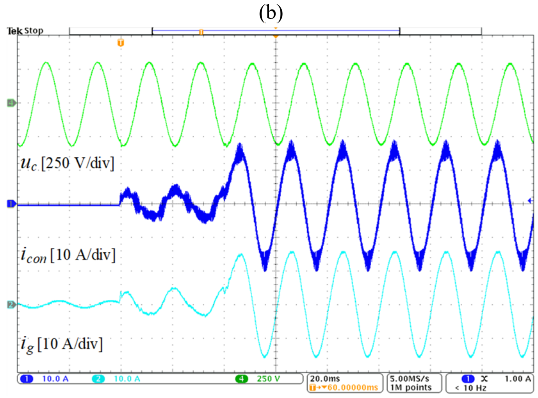

(c)

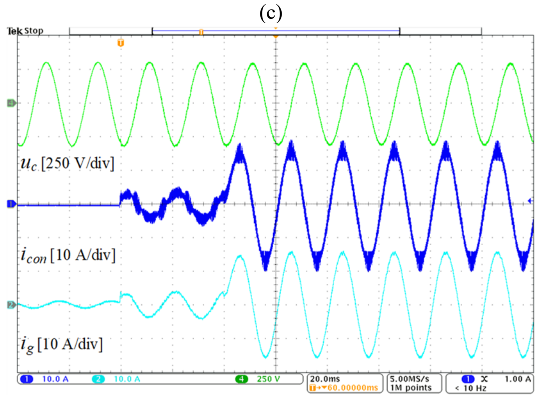

(d)

Fig. 14. Experimental results of LCL Filter-II under an ideal grid condition. (a) Double-sampling CCAD with nominal values of L_1 and C. (b) Double-sampling CCAD with a +20% deviation of L_1 and C. (c) Double-sampling CCAD and CVF with a +20% deviation of L_1 and C. (d) Eight-sampling CCAD and CVF with a +20% deviation of L_1 and C.

is far away from the critical frequency (1333 Hz). Then the intersection frequency between $Y_{o,con}(s)$ and $Y_{g,eq}(s)$ will not be located in the negative-real-part region. Consequently, the parameter deviation of L_1 and C only affects the VSC-grid interactive stability, which is determined by the intersection point between the VSC output admittance $Y_o(s)$ and the grid admittance $Y_g(s)=sC_g+1/sL_g$.

Bode plots of $Y_o(s)$ and $Y_g(s)$ are depicted in Fig. 15 for various cases. The system can be stabilized with the double-sampling CCAD, considering nominal values of L_1 and C. With a +20% deviation of L_1 and C, $Y_o(s)$ intersects with $Y_g(s)$ in its negative-real-part region, which leads to a -24.4° PM and destabilizes the system. By adding the CVF, the dissipativity near the critical frequency is enhanced. However, the non-dissipative region still exists close to the switching frequency, and the system is destabilized by a -2.6° PM. After implementing the proposed eight-sampling control scheme, the dissipation range can be extended up to the switching frequency and the system is stabilized.

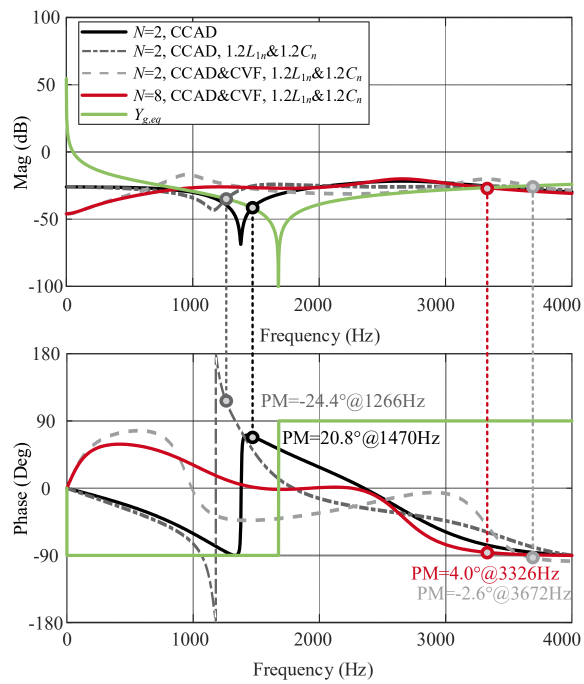

Fig. 15. VSC output admittance seen from PCC $Y_o(s)$ with L_g=3 mH and C_g=3 μF. (CCAD: capacitor current active damping, CVF: capacitor voltage feedforward, N=2: double-sampling, N=8: eight-sampling).

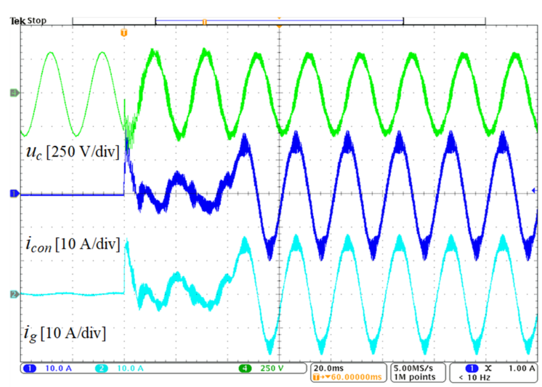

(a)

This article has been accepted for publication in IEEE Transactions on Power Electronics. This is the author's version which has not been fully edited and content may change prior to final publication. Citation information: DOI 10.1109/TPEL.2022.3218378

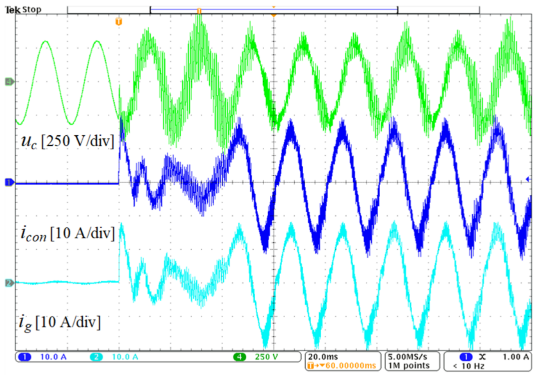

(b)

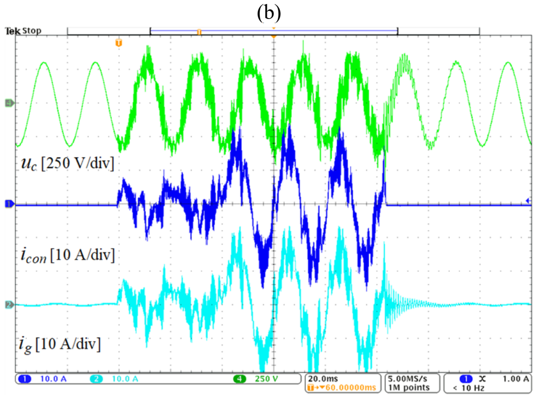

(c)

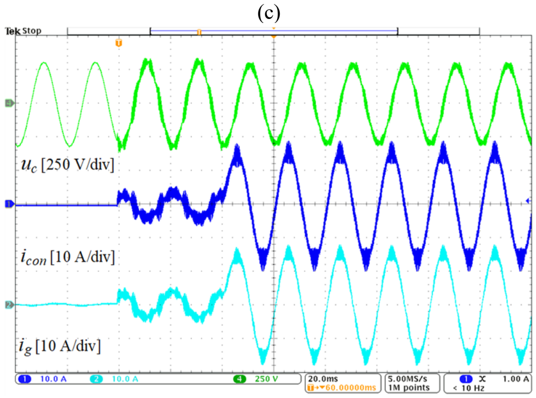

(d)

Fig. 16. Experimental results of LCL Filter-I under a combination of L_g and C_g (L_g=3 mH and C_g=3 μF). (a) Double-sampling CCAD with nominal values of L_1 and C. (b) Double-sampling CCAD with +20% deviation of L_1 and C. (c) Double-sampling CCAD and CVF with +20% deviation of L_1 and C. (d) Eight-sampling CCAD and CVF with +20% deviation of L_1 and C.

According to the experimental result depicted in Fig. 16(a), the system remains stable with the double-sampling CCAD and the nominal value of L_1 and C. However, the system becomes unstable if a +20% deviation of L_1 and C is considered, as shown in Fig. 16(b). With the additional CVF, the system still loses stability due to the non-dissipative region in the high-frequency range, as illustrated in Fig. 16(c). After implementing the proposed multi-sampling control with the CCAD and CVF, the system can be stabilized even with +20% parameter deviations, as depicted in Fig. 16(d).

C. Current reference step response

The operations for a power step change are presented in Fig. 17 using the proposed eight-sampling CCAD and CVF. In the first case, the LCL-Filter I is used under a combination of L_g and C_g (L_g=3 mH and C_g=3 μF). The system can remain

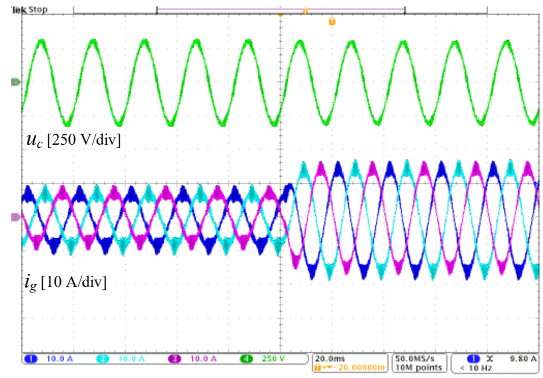

(a)

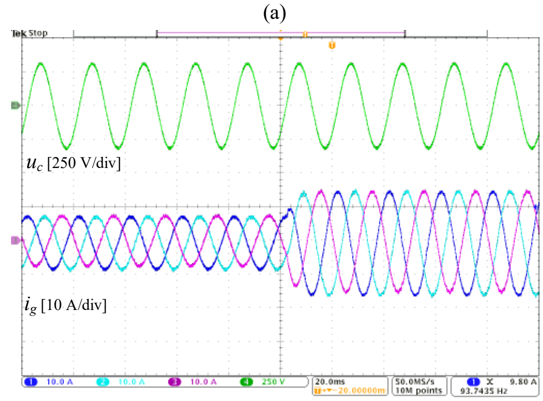

(b)

Fig. 17. Reference current step change performance using the proposed eight-sampling CCAD and CVF with +20% deviation of L_1 and C. (a) Reference current step change using LCL Filter-I under a combination of L_g and C_g (L_g=3 mH and C_g=3 μF). (b) Reference current step change using LCL Filter-II without grid impedance.

stable when the reference current steps from half load (7.5 A) to full load (15 A), as shown in Fig. 17(a). Besides, there is almost no current overshoot during the transient, thanks to the CVF. In the second case, the LCL-Filter II is used without grid impedance, to validate the control internal stability as introduced previously. The system can also operate stably with almost no current overshoot, as shown in Fig. 17(b). It can be concluded that the proposed method can work well under the steady-state and transient situations. In addition, the dissipativity under a distorted grid should be further analyzedin the future work, because the compensate angle for the multi-resonant controllers strongly depends on the active damping structure [31].

VI. Conclusion

This paper investigates the dissipativity robustness against filter parameter deviations for LCL-filtered grid-connected VSCs using grid-side current control. When using double-sampling CCAD, the dissipativity near the critical frequency becomes vulnerable if there is a filter parameter deviation. To tackle this challenge, an additional CVF is implemented to enhance the dissipativity near the critical frequency, which can also improve the transient performance. However, a non-dissipative region is inevitable in the high-frequency region with the double-sampling control. By further utilizing the multi-sampling control, the dissipative region can be optimized up to the switching frequency, so that wideband

This article has been accepted for publication in IEEE Transactions on Power Electronics. This is the author's version which has not been fully edited and content may change prior to final publication. Citation information: DOI 10.1109/TPEL.2022.3218378

resonances can be eliminated. Further, the internal stability can be secured by using the proposed multi-sampling control scheme, which simplifies the LCL-filter design to even allow setting the resonant frequency near the critical frequency. Finally, the proposed method is validated with various cases through the experiments.

REFERENCES

[1] B. Kroposki, B. Johnson, Y. Zhang, V. Gevorgian, P. Denholm, B. Hodge, and B. Hannegan "Achieving a 100% renewable grid: operating electric power systems with extremely high levels of variable renewable energy," *IEEE Power Energy Mag*., vol. 15, no. 2, pp. 61–73, Mar. 2017.

[2] F. Blaabjerg, Y. Yang, D. Yang, and X. Wang, "Distributed power generation systems and protection," *Proc. IEEE*, vol. 105, no. 7, pp. 1311-1331, July 2017.

[3] Z. Yang, C. Shah, T. Chen, J. Teichrib, and R. De Doncker, "Virtual damping control design of three-phase grid-tied PV inverters for passivity enhancement," *IEEE Trans. Power Electron*, vol. 36, no. 6, pp. 6251-6264, June 2021.

[4] D. Zhou and F. Blaabjerg, "Bandwidth oriented proportional-integral controller design for back-to-back power converters in DFIG wind turbine system," *IET Renew. Power Gener*., vol. 11, no. 7, pp. 941-951, June 2017.

[5] B. Wen, D. Boroyevich, R. Burgos, P. Mattavelli, and Z. Shen, "Analysis of D-Q small-signal impedance of grid-tied inverters," *IEEE Trans. Power Electron*, vol. 31, no. 1, pp. 675-687, Jan. 2016.

[6] X. Wang and F. Blaabjerg, "Harmonic stability in power electronic-based power systems: concept, modeling, and analysis," *IEEE Trans. Smart Grid*, vol. 10, no. 3, pp. 2858-2870, May 2019.

[7] W. Wu, Y. Liu, Y. He, H. Chung, M. Liserre, and F. Blaabjerg, "Damping methods for resonances caused by LCL-filter-based current-controlled grid-tied power inverters: an overview," *IEEE Trans. Ind. Electron*., vol. 64, no. 9, pp. 7402-7413, Sep. 2017.

[8] J. Sun, "Impedance modeling and analysis of grid-connected voltage-source converters," *IEEE Trans. Power Electron*, vol. 26, no. 11, pp. 3075-3078, Nov. 2011.

[9] J. Ma, X. Wang, F. Blaabjerg, L. Harnefors, and W. Song, "Accuracy analysis of the zero-order hold model for digital pulse width modulation," *IEEE Trans. Power Electron.*, vol. 33, no. 12, pp. 10826-10834, Dec. 2018.

[10] Y. Gu, W. Li, and X. He, "Passivity-based control of dc microgrid for self-disciplined stabilization," *IEEE Trans. Power Syst*., vol. 30, no. 5, pp. 2623–2632, Sep. 2015.

[11] L. Harnefors, X. Wang, A. Yepes, and F. Blaabjerg, "Passivity-based stability assessment of grid-connected VSCs-An overview," *IEEE J. Emerg. Sel. Top. Power Electron*., vol. 4, no. 1, pp. 116–125, Mar. 2016.

[12] A. Akhavan, H. Mohammadi, J. Vasquez, and J. Guerrero, "Passivity-based design of plug-and-play current-controlled grid-connected inverters," *IEEE Trans. Power Electron*., vol. 35, no. 2, pp. 2135-2150, Feb. 2020.

[13] X. Wang, F. Blaabjerg, and P. Loh, "Passivity-based stability analysis and damping injection for multiparalleled VSCs with LCL filters," *IEEE Trans. Power Electron*., vol. 32, no. 11, pp. 8922-8935, Nov. 2017.

[14] C. Xie, K. Li, J. Zou, and J. Guerrero, "Passivity-based stabilization of LCL-type grid-connected inverters via a general admittance model," *IEEE Trans. Power Electron*., vol. 35, no. 6, pp. 6636-6648, 2020.

[15] C. Xie, J. Zou, D. Liu, and J. Guerrero "Passivity-based design of grid-side current-controlled LCL-type grid-connected inverters," *IEEE Trans. Power Electron*., vol. 35, no. 9, pp. 9813-9823, 2020.

[16] X. Wang, Y. He, D. Pan, H. Zhang, Y. Ma, and X. Ruan, "Passivity enhancement for LCL-filtered inverter with grid current control and capacitor current active damping," *IEEE Trans. Power Electron*., vol. 37, no. 4, pp. 3801-3812, April 2022.

[17] H. Chen, P. Cheng, X. Wang, and F. Blaabjerg, "A passivity-based stability analysis of the active damping technique in the offshore wind farm applications," *IEEE Trans. Ind. Appl*., vol. 54, no. 5, pp. 5074-5082, Oct. 2018.

[18] S. Zhou, X. Zou, D. Zhu, L. Tong, and Y. Kang, "Improved capacitor voltage feedforward for three-phase LCL-type grid-connected converter to suppress start-up inrush current," *Energies*, vol. 10, no. 5, p. 713, May 2017.

[19] A. Nazib, D. Holmes, and B. McGrath, "Enhanced transient performance of a self-synchronising inverter during start up and severe grid fault conditions," in *Proc. IEEE ECCE Asia*, pp. 1167-1174, March 2021.

[20] S. He, D. Zhou, X. Wang, and F. Blaabjerg, "A review of multi-sampling techniques in power electronics applications," *IEEE Trans. Power Electron*., vol. 37, no. 9, pp. 10514-10533, Sept. 2022.

[21] X. Zhang, P. Chen, C. Yu, F. Li, H. Do, and R. Cao, "Study of a current control strategy based on multisampling for high-power grid-connected inverters with an LCL filter," *IEEE Trans. Power Electron*., vol. 32, no. 7, pp. 5023-5034, July 2017.

[22] S. He, D. Zhou, X. Wang, and F. Blaabjerg, "Aliasing suppression of multi-sampled current-controlled LCL-filtered inverters," *IEEE J. Emerg. Sel. Top. Power Electron.*, vol. 10, no. 2, pp. 2411-2423, April 2022.

[23] S. He, D. Zhou, X. Wang, and F. Blaabjerg, "Line voltage sensorless control of grid-connected inverters using multisampling," *IEEE Trans. Power Electron.*, vol. 37, no. 4, pp. 4792-4803, April 2022.

[24] S. Golestan, J. M. Guerrero, and A. M. Abusorrah, "MAF-PLL with phase-lead compensator," *IEEE Trans. Ind. Electron*, vol. 62, no. 6, pp. 3691-3695, June 2015.

[25] L. Harnefors, L. Zhang, and M. Bongiorno, "Frequency-domain passivity-based current controller design," *IET Power Electron*., vol. 1, no. 4, pp. 455–465, Dec. 2008.

[26] C. Wang, X. Wang, Y. He, and X. Ruan, "A passivity-based weighted proportional-derivative feedforward scheme for grid-connected inverters with enhanced harmonic rejection ability," *IEEE J. Emerg. Sel. Top. Power Electron.*, *early access*, 2022.

[27] D. Pan, X. Ruan, C. Bao, W. Li, and X. Wang, "Optimized controller design for LCL-type grid-connected inverter to achieve high robustness against grid-impedance variation," *IEEE Trans. Ind. Electron*., vol. 62, no. 3, pp. 1537–1547, Mar. 2015.

[28] Y. He, X. Wang, X. Ruan, D. Pan, X. Xu, and F. Liu, "Capacitor-current proportional-integral positive feedback active damping for LCL-type grid-connected inverter to achieve high robustness against grid impedance variation," *IEEE Trans. Power Electron*., vol. 34, no. 12, pp. 12423–12436, Dec. 2019.

[29] M. Zabaleta, E. Burguete, D. Madariaga, I. Zubimendi, M. Zubiaga, and I. Larrazabal, "LCL grid filter design of a multi-megawatt medium-voltage converter for offshore wind turbine using SHEPWM modulation," *IEEE Trans. Power Electron*., vol. 31, no. 3, pp. 1993–2001, Mar. 2016.

[30] Y. Tang, W. Yao, P. Loh, and F. Blaabjerg, "Design of LCL filters with LCL resonance frequencies beyond the Nyquist frequency for grid-connected converters," *IEEE J. Emerg. Sel. Top. Power Electron*, vol. 4, no. 1, pp. 3-14, March 2016.

[31] L. Harnefors, A. Yepes, A. Vidal, and J. Gandoy, "Passivity-based controller design of grid-connected VSCs for prevention of electrical resonance instability," *IEEE Trans. Ind. Electron*., vol. 62, no. 2, pp. 702-710, Feb. 2015.